communications physics

A Nature Portfolio journal

Article

https://doi.org/10.1038/s42005-025-02393-7

Increasing rare earth extraction kinetics by tailored magnetic fields

Kilian Ortmann[1], Alexander Bidmon[2,3], Kerstin Eckert[1,2] & Zhe Lei[1,2]

The separation of the chemically similar rare-earth (RE) elements is difficult, consumes large amounts of chemicals, energy, water and emits environmentally harmful substances. To enhance the efficiency of RE separation, we develop and validate a magnetic-assisted solvent extraction method. For that purpose, we use a Hele-Shaw configuration and investigate the Dysprosium (Dy) cation exchange across a water-oil interface in the presence of a millimeter-sized NdFeB magnet. The tailored magnetic field introduces a Kelvin force that drives solutomagnetic convection if the modified Rayleigh number, Ra^*, exceeds the critical value $Ra^* \sim 5 \times 10^6$. This convection continuously replenishes Dy(III)-depletion at the interface with fresh solution from bulk. The resulting enhancement in extraction kinetics, expressed by the Sherwood number, scales nearly quadratically with Ra^*. This magnetic field-driven intensification enables more efficient bulk separation of heavy RE and could potentially provide a greener separation route with superior selectivity.

The rare earth (RE) elements are a group of 17 elements in the periodic table including the lanthanide elements, yttrium and scandium. Their unique magnetic[1,2], catalytic[3] and phosphorescent[4,5] properties have enabled a broad spectrum of high-tech applications[6]. The world's ambition to achieve cleaner energy and climate neutrality[7] will further boost the demand for rare-earth significantly[8]. This is reflected by the stable 17% increase in the RE oxides production rate over the past 5 years, reaching 30 kilotons in 2022[9]. Despite the importance of rare earths, their recycling rates are only at 1%[10]. Their supply relies mostly on primary resources[11] processing of which is associated with adverse environmental footprints[12]: 1 ton of RE generates e.g. 2,000 tons of toxic waste material, 1000 tons of heavy metal laden waste water or 40−110 tons of CO_2[13]. The development of a circular economy for rare earths through technological innovations holds considerable potential for overcoming these challenges and securing the growing market demand[13].

Rare-earths are relatively abundant with 120 million tons of reserves in the earth's crust worldwide. Rare-earth elements appear in mixed deposits which require dedicated separation processes involving solvent extraction, a method used since the 1960 s[14,15]. The trivalent RE ions, RE(III), have very similar binding affinity with any given ligand, called extractant, used during the solvent extraction process. Hence, separation relies on the small differences in their respective equilibrium partitioning ratio between the RE-complex loaded in the organic phase and the RE(III) in the aqueous raffinate, known as distribution coefficient. Therefore, only very limited mean separation factors, referring to the ratio of the distribution coefficient for different RE(III)s, between neighboring rare earth elements can be realized: less than three in the best case, for the cation-exchanging extractant D2EHPA (di-2-ethylhexylphosphoric acid). Thus to achieve a high degree of purity, a large number, up to one thousand, of mixer-settler stages needs to be employed[11]. Consequently, huge amounts of costly extractants and organic solvents, as well as mineral acid and water are required, further exacerbating the burden on the environment[16]. Alternative resources[17] with innovative separation methods have been intensively explored[18], such as green solvent in solvometallurgy[19], RE(III)-sensitive bacteria[20], ligands with high selectivity[21,22], RE(III) magnetomigration in gel[23], magnetic separation with evaporation[24] or via a porous medium[25], or the usage of magnetic field to enhance selective crystallization[26]. However, no process has been explored that combines both the features of rapid extraction kinetics for the heavy RE's with reduced consumption of energy and chemicals, while being suitable for a scale-up.

Motivated by this situation, we propose an alternative approach: enhancing the extraction kinetics by introducing a tailored magnetic field into the state-of-art solvent extraction process. We demonstrate that the so-called solutomagnetic convection, spontaneously forming after applying the magnetic field, is the basic tool to enhance the extraction kinetics of heavy RE's, e.g. dysprosium, holmium, terbium, erbium and gadolinium, having high magnetic susceptibilities[27]. In a combination of experiment and simulation we resolve the pattern formation, associated with solutomagnetic convection, and the flow transitions therein. Finally, the increase in extraction kinetics caused by solutomagnetic convection is quantified.

[1]Institute of Fluid Dynamics, Helmholtz-Zentrum Dresden-Rossendorf (HZDR), Dresden, D-01328, Germany. [2]Institute of Processing Engineering and Environmental Technology, Technische Universität Dresden, Dresden, D-01069, Germany. [3]Present address: Institute of Fluid Dynamics, Helmholtz-Zentrum Dresden-Rossendorf (HZDR), Dresden, D-01328, Germany. e-mail: Z.Lei@hzdr.de

Results and discussion

Kelvin-force-modulated extraction of rare earth ions

To prove this concept, trivalent dysprosium ions, Dy(III), are used in this study because Dy(III) has the highest molar magnetic susceptibility of all RE(III)s.

Free optical access is provided in the vicinity of the interface thanks to the immobilized organic droplet, which is narrowly confined by two horizontal walls in a Hele-Shaw configuration, see center of Fig. 1. Within this setup, an industrially relevant Dy(III)-PC88A-HCl[11] system is studied. It uses the commercially available extractant, Mono-2-ethylhexyl (2-Ethylhexyl)phosphonate abbreviated to as PC88A, dissolved in paraffin oil. The oil is dispersed as a single droplet in the aqueous Dy(III) solution, which appears as orange circle in Fig. 1. The axial-symmetric droplet has the shape of a quasi-vertically extruded cylinder with outwards bulging sides. At the droplet's interface, a mass transfer occurs due to the cation exchange of the Dy(III) with PC88A according to[28]:

$$Dy^{3+} + 3\overline{H_2A_2} \underset{\text{backward}}{\overset{\text{forward}}{\rightleftharpoons}} \overline{Dy(HA_2)_3} + 3H^+, \quad (1)$$

where H_2A_2 is the dimeric PC88A, and $Dy(HA_2)_3$ is the RE complex extracted into the organic phase. The resulting transport processes of Dy(III) in the aqueous phase are resolved in space and time by means of laser interferometry and laser-induced fluorescent particle image velocimetry (PIV), see Methods. The snapshots arranged along the curved black arrow in Fig. 1 show the measured Dy(III) concentration field at progressive time stamps. The enlarged pictures, at $t = 1$ s and $t = 51$s, compare the behavior with magnetic field (right half) and without magnetic field (left half). The smaller pictures ($t = 5$ s etc.) focus entirely on the development with a magnetic field. Obviously, the extraction kinetics in the latter case is much quicker, visible in the extension of areas in blue shades, corresponding to a depletion of Dy(III) as $\Delta c \sim -3...5$ mM. Most interestingly, blue plume-like structures emerge. We use the timeline at the bottom of Fig. 1 to graphically explain the processes. Prior to $t = 0$ s, when the magnet is applied, the two continuous phases are brought into contact. Cation exchange at the interface, the rate law of which is dominated by the forward reaction in Eq. (1), consumes Dy(III) ions. As a result, a Dy(III) concentration boundary layer is formed at the droplet interface, see the orange curve labeled c. The concentration drop across the boundary layer, Δc, will gradually reduce the extraction kinetics. The stray field $\vec{H}$ of the NdFeB permanent magnet gives rise to a weak magnetization $\vec{M}$ of the Dy(III). Hence a Kelvin force, $\vec{f}_m = \nabla(\mu_0 \vec{H} \cdot \vec{M})$, appears (see Section Governing Equations), μ_0 refers to the vacuum permeability. Note that the Dy(III) solution has paramagnetic properties with negligible demagnetization field.

As no Lorentz force is present, the Kelvin force acting on the Dy(III) solution in the stray field of the permanent magnet is simplified to[1,29,30]

$$\vec{f}_m = \frac{\chi_{sol}}{2\mu_0} \nabla \vec{B}^2 \quad (2)$$

where $\vec{B}$ and χ_{sol} are the magnetic flux density and the magnetic susceptibility of the solution, respectively. The concentric magnet-droplet configuration results in a Kelvin force pointing radially inwards, see red arrows in the bottom line of Fig. 1. The drop of Dy(III) concentration, Δc, across the boundary layer due to the cation exchange, modifies both the magnetic susceptibility, $\chi_{sol} = \chi_{sol,0} + \chi_{Dy}\Delta c$, and the density of the solution, $\rho_c = \rho_0(1 + \alpha(c_0 + \Delta c))$. Thus, the radial concentration variation, see Fig. 1

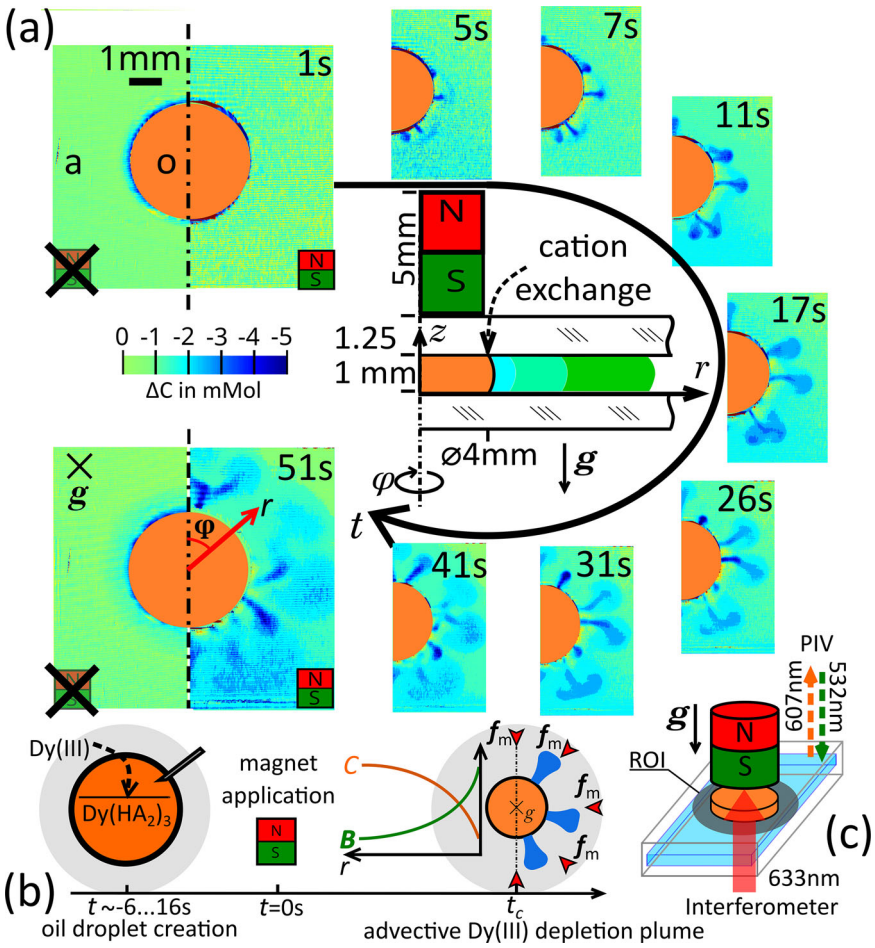

Fig. 1 | Magnetic-assisted solvent extraction experimental setup and validation. a The snapshot sequence along the black arrow quantifies the space-resolved Dy(III) concentration boundary layer in presence of the magnet (initial concentration: 0.5 M Dy(III) and 0.5 M PC88A). The color bar displays the decrease in Dy(III) concentration, Δc between [-5,0] mM, due to Dy(III) mass transfer. The black line shown at 1 s represents the scale bar of 1 mm. The larger snapshots at 1 and 51 s show the differences with and without the magnet in the region-of-interest (ROI) of the camera, which is colored in gray in (**b**). **b** shows schematic diagrams of the droplet within the aqueous phase and the profiles of concentration c (orange) and magnetic field B (green) at the droplet, as well as the experiment procedure along the time arrow: oil droplet injection, magnetic field application and solutomagnetic convection development, as shown in (**a**). The side view of the setup is shown in (**c**) with the organic droplet in an aqueous solution inside the Hele-Shaw cell and the small rod magnet applied on top. This orientation offers optical access to the boundary layer at the aqueous side.

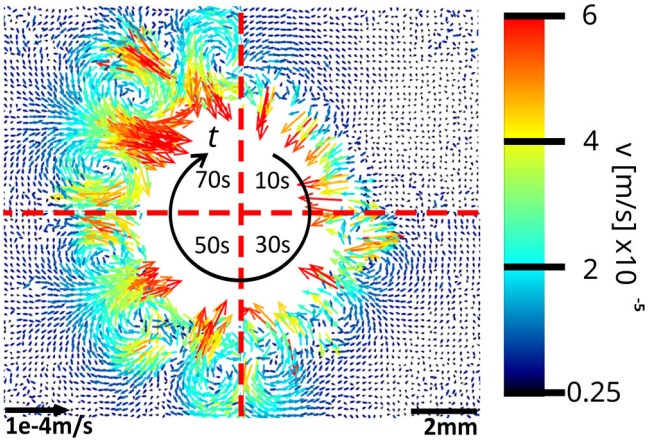

Fig. 2 | Solutomagnetic convection measured by particle image velocimetry. Development of the velocity field around the droplet, measured by PIV, at different time intervals under conditions identical to Fig. 1 with magnet. The snapshots of 10, 30, 50 and 70 s after the application of magnetic field are shown along the curved time axis (t). The composite image is divided into four quadrants by red dashed lines centered at the droplet. Each quadrant shows one quarter of the whole velocity field at the specified time step. The colorbar denotes the absolute velocity in between [0.025, 0.06] mm/ s. The black line represents the scale bar of 2 mm.

bottom, imposes a proportional variation of the magnetic susceptibility, χ_{sol}. As this occurs in the presence of an anti-parallel magnetic field stratification, the curl of the Kelvin force in Eq. (2) is non-zero. Hence, the Kelvin forces is able to drive a convection, the so-called solutomagnetic convection shown in Fig. 2. Beside the topology of the magnetic field, it is essential that the strong field gradient, $\nabla\vec{B}^2$, covers the characteristic length scale of the Dy(III) boundary layer, see Section *Methods* - Scaling factors and dimensionless governing equations. Only with such a tailored magnetic field can solutomagnetic convection be induced and the extraction kinetics improved. A generalization of the magnetic field effect will be discussed in the next section.

With this background we examine the behavior Fig. 1 with and without the magnet more closely. If no magnetic field is present, the Dy(III) concentration boundary layer remains axially symmetric, resembling a diffusive-like pattern. Strong deviations from this pattern occur in presence of the magnet: after t = 5 - 10 s, the depleted Dy(III) concentration boundary layer loses its axial symmetry. Plume-shape structures (in blue) propagate radially outwards. The number of plumes, 8 ± 2, along the droplet perimeter varies statistically for all concentration pairs studied. Within 10–20 s the plumes propagate over a distance of about 2 mm radially away from the interface. Afterwards, the head of the plume starts to expand in angular direction to a length of up to 3 mm. The resulting depletion of the solution is reflected by a lighter blue in the color scale of Fig. 1. The plumes are similar to the structures typically observed in Rayleigh-Bénard convection (RBC)[31]. Unlike RBC where the density change due to a vertical thermal stratification drives the flow, the magnetic field and the change of magnetic susceptibility due to a radial concentration stratification play the main role in the present case.

The evolution of the velocity field, underlying the processes in Fig. 1, is shown in Fig. 2, based on PIV measurements in the horizontal plane. At the beginning, t = 10 s, all velocity vectors point radially inwards with a similar intensity. Thus in the upper part of the Hele-Shaw cell, the flow is towards the interface. By continuity, this forces a flow away from the interface at bottom as shown in the numerical simulations presented later. Since the camera isfocused onto the top plane, z = 1 mm, the imaging of the tracer particles in the PIV interrogation window is sharper compared to that from the bottom - the bottom flow is not accessible by cross correlation[32].

The radially inward motion on top signals that the buoyancy-driven convection is negligible - the latter would imply a flow in opposite direction as the Dy(III) depleted solution is lighter. In the velocity field belonging to t = 30 s, a break in the axial symmetry is clearly visible. Pairs of vortices emerge, rotating counter- and clockwise. With progressing time, the radial velocity of this vortex structure increases. Interestingly, this stabilizes the flow structure until a quasi-steady state is reached beyond t = 70 s.

Fundamental differences exist between the present magnetic-assisted solvent extraction and evaporation-assisted magnetic separation[24,27,30,33]. First, the source of the Dy(III) concentration boundary layer is cation exchange instead of solvent evaporation. Second, Dy(III) is depleted at the interface rather than being enriched. Thus, in the present case the radial component of the Kelvin force actively pushes fresh Dy(III) solution from bulk towards interface. If certain critical conditions are exceeded, later quantified in terms of the Rayleigh* number, an instability occurs. The instability causes a break in the axial symmetry. As a result, the plume-like structure emerges, which eventually leads to a larger-scale recirculation around the droplet; cf. Fig. 2, t = 70 s.

Numerical simulations of solutomagnetic convection

To capture the flow structures, shown in two dimensions in Fig. 2, three-dimensional (3D) numerical simulations are performed, using the Navier-Stokes equation and the transport equation for the active scalar, c, in Boussinesq approximation[33]:

$$\partial_t\vec{u} + \vec{u}\cdot\nabla\vec{u} = -\frac{1}{\rho_{c_0}}\nabla p' + \nu\nabla^2\vec{u} - \frac{1}{\rho_{c_0}}\nabla(e_{pot})\Delta c \tag{3}$$

$$\partial_t c + \vec{u}\cdot\nabla c = \kappa_c\nabla^2 c. \tag{4}$$

Here $p\prime$, ν and κ_c, refer to reduced pressure, kinematic viscosity and mass diffusivity. Momentum and mass boundary condition are detailed in the Section *Methods*. The gradient of the potential energy density field

$$e_{\mathrm{pot}} = -\left(\frac{\chi_{\mathrm{Dy}}}{2\mu_0}\cdot\vec{B}^2 + \rho_0 g\alpha\cdot z\right) + \mathrm{const}, \tag{5}$$

describes the forcing by Kelvin force and buoyancy per unit Dy(III) concentration.

The numerically simulated 3D Dy(III) concentration field in the Hele-Shaw cell is presented in Fig. 3a, b in two perspectives at progressive time stamps. Fig. 3a shows the view from the bottom. While at t = 70 s the boundary layer is still axially symmetric in the numerical simulations, it starts bulging at t = 90 s. This is the fingerprint of the break of symmetry. From the bulged zone, a plume of depleted Dy(III) solution is ejected. The plume starts to expand radially outward over a distance of about 1 mm away from the interface, similar to what was observed experimentally. Fig. 3

b shows the same sequence in the plane perpendicular to Fig. 3a in side view along the dashed red line at φ = 0. Surprisingly, even under condition of axial symmetry at $t \le 70$ s, a nonlinear stratification along the gravitational direction, is already formed. Due to the radially inward-pointing Kelvin force, the Dy(III) concentration boundary layer is squeezed to a thickness of 0.3 mm. At the bottom, that is, at position z = 0 mm, the depleted solution is stretched radially outward, cf. Fig. 3 (70 s). This is caused by the reduction of the stray field $\vec{B}$-intensity with increasing distance from the rod magnet. When the Dy(III) depletion plume has propagated over a distance of 1 mm along the bottom, it starts to stratify vertically upwards. After the break of axial symmetry, the expansion along the radial direction accelerates. Beyond t = 110 s an increasingly stable vertical density stratification is formed at the top region as a result of the gravitational force acting on the lighter solution depleted in Dy(III). Although simulation and experiment agree very well, the break of symmetry in the simulation happens with a delay of 80 s compared to the experiments. The reason is seen in unavoidable deviations imposed by the experimental procedure. For instance, the injection of the organic phase at $t < 0$ s pushes the aqueous phase radially outwards. This causes a weak convection already prior to the application of the magnet at t = 0.

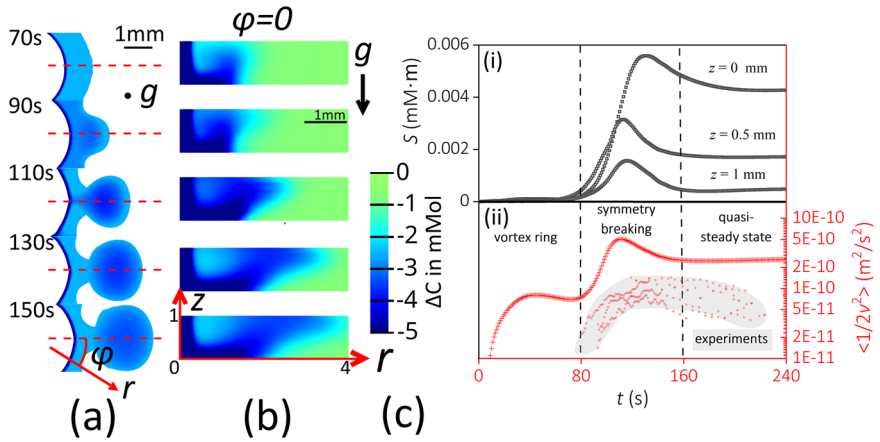

Fig. 3 | Symmetry breaking of Dy(III) concentration boundary layer by a magnetic field. 2D projections of the simulated 3D Dy(III) concentration boundary layer: (**a**) bottom view of the horizontal ($\varphi - r$) plane, perpendicular to the vector of gravitational acceleration g, with r as the radial distance from the droplet interface and φ as the azimuth angle. **b** cross-section along the radial axis r showing a side view through the center of a single plume along the dashed line in (**a**) at angle $\varphi = 0$. The color bar covers the Dy(III) depletion in between [-5, 0] mM. The black line shown at 90 s represents the scale bar of 1 mm. **c** Temporal evolution of the similarity measure, $S = < \frac{1}{2}\sum_{i=4}^{i=1}(r_i\Delta c_i + 1 - r_{i+1}\Delta c_i) > \sum$, at different depths, $z = 0$, 0.5, and 1 mm, see coordinate system in (**b**) in the image (i) above and of the average kinetic energy, $e_{kin} = < 1/2v^2 >$ in the image (ii) below: numerical simulation (red cross shaped markers) vs. experiment (red data cloud overlaid on gray background rendering).

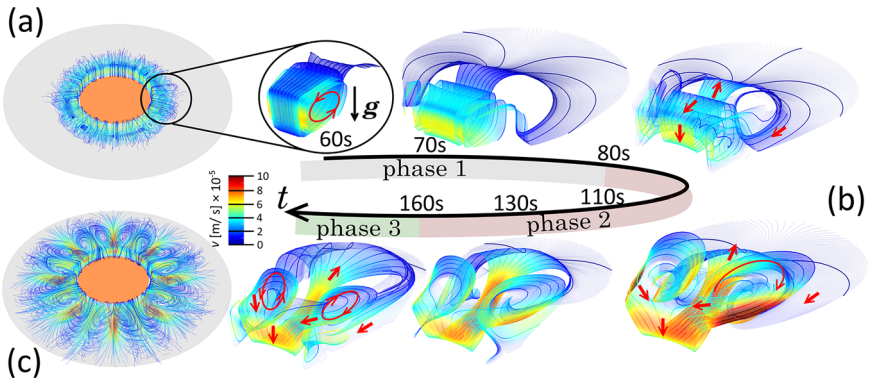

Fig. 4 | Three phases of solutomagnetic convection. Numerical simulation of the solutomagnetic convection: time-resolved 3D structure of the velocity field. **a**, **c** show the initial vortex ring (phase 1) around the droplet (rendered artificially in orange) and the final a quasi-steady state (phase 3), respectively. The snapshots in (**b**) around the curved arrow (t-axis) provide a zoom into the streamlines also detailing the symmetry break (phase 2) between $t = 60$ and 160 s. The transition from the first vortex-ring state (phase 1) towards the quasi-stead state (phase 3) occurs via symmetry breaking (phase 2).

To quantitatively describe the onset and degree of the symmetry break, we conduct time-resolved similarity measures for the Dy(III) concentration field sampled in the r-ϕ-space at different depths, i.e., z-positions. For that purpose, we use the discrete sum of the area method[34], quantified by the value $S = < \frac{1}{2}\sum_{i=4}^{i=1}(r_i\Delta c_i + 1 - r_{i+1}\Delta c_i) > \sum$, see Section *Methods*. S is equivalent to the enclosed area of sampling in $\Delta c - r$ space between $\phi = 0$ and $\phi = \frac{\pi}{4}$. The value $S = 0$ means that the concentration profile is axially symmetrical, see Fig. 3c.

The numerically simulated velocity field is represented in Fig. 4 in terms of the streamlines. Three different phases are identified in excellent agreement with the experiment. In particular, their 3D structures are resolved, which are not accessible from experiments.

Phase 1: vortex ring

During this initial stage, the extraction kinetics, dominated by the forward reaction in Eq. (1), is at it's maximum. The gradually established concentration boundary layer, in presence of the magnetic field, causes solutomagnetic convection, which starts to build up at the vicinity of the interface. While the concentration field remains axially symmetrical, reflected by a vanishing similarity measure, S, at different vertical depths (cf. Fig. 3c), the velocity field is confined to a narrow region of 1.5 mm radially outward from the interface. The streamline at $t = 60$ s shows that the convection is dominated by a toroidal super-structure, labeled as the vortex ring in Fig. 3c. The evolution of the vortex ring is quantified in terms of the averaged kinetic energy, $< 1/2v^2 >$, plotted in Fig. 3c. During vortex formation the kinetic energy rises and reaches a quasi-steady state between $t \in [30, 80]$ s before symmetry breaking sets in.

Phase 2: symmetry breaking

Signs of axial symmetry breaking are clearly visible in the similarity measurement. At $t = 80$ s the flow field starts to deviate from the vortex ring structure. Similarly to the PIV observation, this is a highly dynamic period reflected by a steep rise of the kinetic energy, $e_{kin} = < 1/2v^2 >$. Vortex pairs rotating counter- and clockwise are clearly visible after $t = 90$ s. The dimensions have the same aspect ratio as illustrated in Fig. 1 middle insertion, e.g. the vortex length is 1 mm along gravitational direction near interface. At a distance of 1.5 mm radially from the interface, the Dy(III) depleted solution is advected outward and upwards from the bottom plane. At the same time, fresh Dy(III) solution is advected from the bulk radially inwards. Before it reaches the interface, it passes a pre-mixed zone in which the vortex pairs are located. In total, eight such vortex pairs are found in the simulations which develop over a timespan of 60 s toward a maximum diameter of 4–5 mm. This agrees excellently with the experiments where 8 ± 2 vortex pairs have been found with very similar features. The only difference is the differing value of the kinetic energy, cf. Fig. 3c, as the interfacial region cannot be resolved for two reasons: First, the curved droplet interface blocks the direct optical access to the ca. 0.4 mm thick layer which directly surrounds the interface. Second, the tracer particles undergo

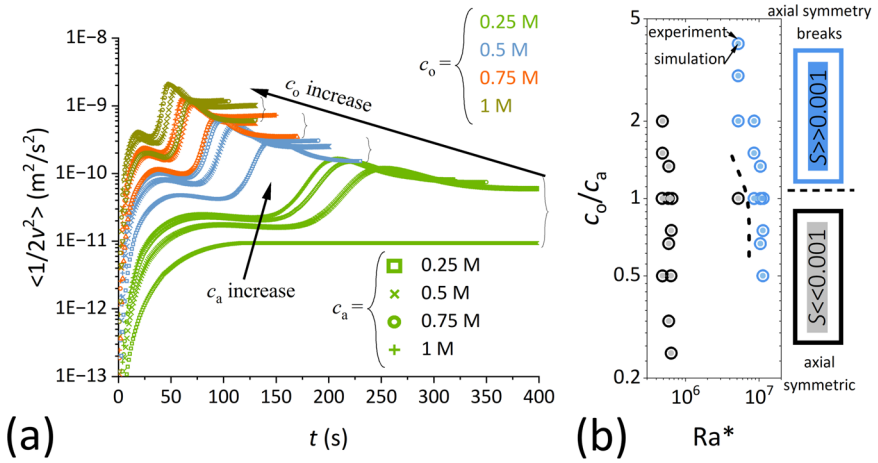

Fig. 5 | Symmetry breaking and its statistics. a shows the evolution of the kinetic energy e_{kin} at varying initial concentration of Dy(III) (c_a, grouped into symbol shapes) and PC88A (c_o, grouped into symbol colors). Phase 1, corresponding to vortex ring formation is evident for all cases through an initial rapid increase in e_{kin}. A second rapid increase in e_{kin} occurs only at higher c_a and c_a (except when they are both 0.25 M). Once the symmetry breaking criterion is met, a second growth of e_{kin} emerges due to symmetry breaking, followed by a decline toward a higher quasi-steady state level compared to the vortex ring phase. **b** Axial-symmetry breaking criteria diagram plotted in the Ra* - c_o/c_a space. The colors represent the similarity measure S, detailed in Methods. A similarity measure in gray [blue] indicates [broken] axial symmetry. The dashed line separating the black and blue data clouds mark the border between these two states. A clear threshold of $s = 0.001$ is used to determine the onset of symmetry breaking: value above this threshold ($S >> 0.001$) are shown in blue, indicating broken axial symmetry, whereas values well below it ($S << 0.001$) appear in gray, indicating preserved symmetry.

both diffusiophoresis[35] and magnetophoresis[36]. As a result, the tracer particle density gradually diminishes near the interface, which deteriorates the statistics of e_{kin} in Fig. 3.

Phase 3: quasi-steady state

After a transient phase of about 80 s, a time-independent quasi-steady flow field is established at $t = 160$ s. The streamline at $t = 160$ s displays a large-scale re-circulation zone with a radially confined convection. This flow structure governs the transport of diluted Dy(III) solution away from the concentration boundary layer, and the transport of fresh Dy(III) from the bulk towards the interface. This stage is characterized by a rather constant kinetic energy and a gradually reduced similarity measure Fig. 3c. Thus, there is a stable advective process which continuously enhances the extraction kinetics.

Scaling law for the magnetic-assisted REE extraction rate

We next examine how the flux of Dy(III) ions from the aqueous towards the organic phase scales with the magnetic field during the quasi-steady extraction kinetics in phase 3. For that purpose, Navier-Stokes and transport equations are nondimensionalized (cf. Section *Governing equations*):

$$\frac{1}{Sc}(\partial_t \vec{\tilde{u}} + \vec{\tilde{u}} \cdot \nabla \vec{\tilde{u}}) = -\nabla \tilde{p} + \nabla^2 \vec{\tilde{u}} + \mathrm{Ra}^* \cdot \tilde{c} \cdot \vec{e}_{-\nabla(e_{pot})} \quad (6)$$

[30,33]

$$\partial_t \tilde{c} + \vec{\tilde{u}} \cdot \nabla \tilde{c} = \nabla^2 \tilde{c} \quad (7)$$

where $\vec{\tilde{u}}$, $\tilde{p}$ and $\tilde{c}$ refer to dimensionless velocity, pressure and concentration, respectively, introduced in Section *Governing equations*. Ra* refers to the dimensionless Rayleigh* number,

$$\mathrm{Ra}^* = \frac{L_c^3 \cdot c_0 |\nabla e_{pot}|}{\rho_{c_0} \cdot \nu D}. \quad (8)$$

It specifies the ratio of the time scales of the dissipative effects, mass diffusion and viscosity, to those forced by Kelvin force and buoyancy. Both enter into the potential energy density field, e_{pot}, given in Eq. (5). It is worthy noticing that when the magnetic flux density disappears, Ra* is reduced to the conventional Rayleigh number in Rayleigh-Bénard convection.

The primary goal now is to find how the dimensionless analog of the flux of Dy(III) ions, namely the Sherwood number

$$\mathrm{Sh} = \frac{L_c V \cdot \partial_t < c >}{c_0 \cdot A \cdot D}, \quad (9)$$

scales with the relevant dimensionless quantities, which are the concentration ratio c_o/c_a, Ra^* and Schmidt number, $Sc = \nu/D$.

To establish this scaling, a parametric variation of the initial concentrations of Dy(III) and extractant (PC88A), c_a and c_o, is done in the range from 0.25 M to 1 M, and plotted in Fig. 5a. The shape of the curves is already known from Fig. 3c. When the axi-symmetry of the vortex ring (phase 1) is broken (phase 2), the kinetic energy of the quasi-steady state (phase 3) runs into a plateau. In Fig. 5a, a clear trend towards an increase e_{kin} in this quasi-steady state is found with increasing c_o, which has a greater influence than c_a. At the smallest concentrations, $c_a = c_o = 0.25$ M (lower green line), the symmetry breaking is no longer found. By systematically reducing Ra* by allowing a 1.5 mm gap between the magnet pole and the cuvette wall, see Section *Methods*, the phase space of the system, c_o/c_a vs. Ra*, is established in Fig. 5b. In very good agreement with the experiments, a clear separation of states with and without axial symmetry is visible and marked by the dashed line separating the blue and black data clouds. Thus, a critical Ra* number, $\mathrm{Ra}^*_{cr} \sim 5 \times 10^6$, can be derived at which the break of axial symmetry occurs. The resulting large-scale circulation effectively enhances the extraction kinetics of Dy(III).

In the quasi-steady state phase 3, the Reynolds number, $\mathrm{Re} = \frac{L_c \cdot (2 < v^2/2 >)^{0.5}}{\nu}$, and the Sherwood number, Eq. (9), show a dependence which is depicted in Fig. 6.

Using multi-dimensional linear regression we obtain:

$$\mathrm{Re} = 1.91 \times 10^{-12} \left(\frac{c_o}{c_a}\right)^1 \cdot \mathrm{Ra}^{*1.48} \cdot \mathrm{Sc}^{0.29} \quad (10)$$

$$\mathrm{Sh} = 1.38 \times 10^{-23} \left(\frac{c_o}{c_a}\right)^{2.1} \cdot \mathrm{Ra}^{*2.14} \cdot \mathrm{Sc}^{2.37} \quad (11)$$

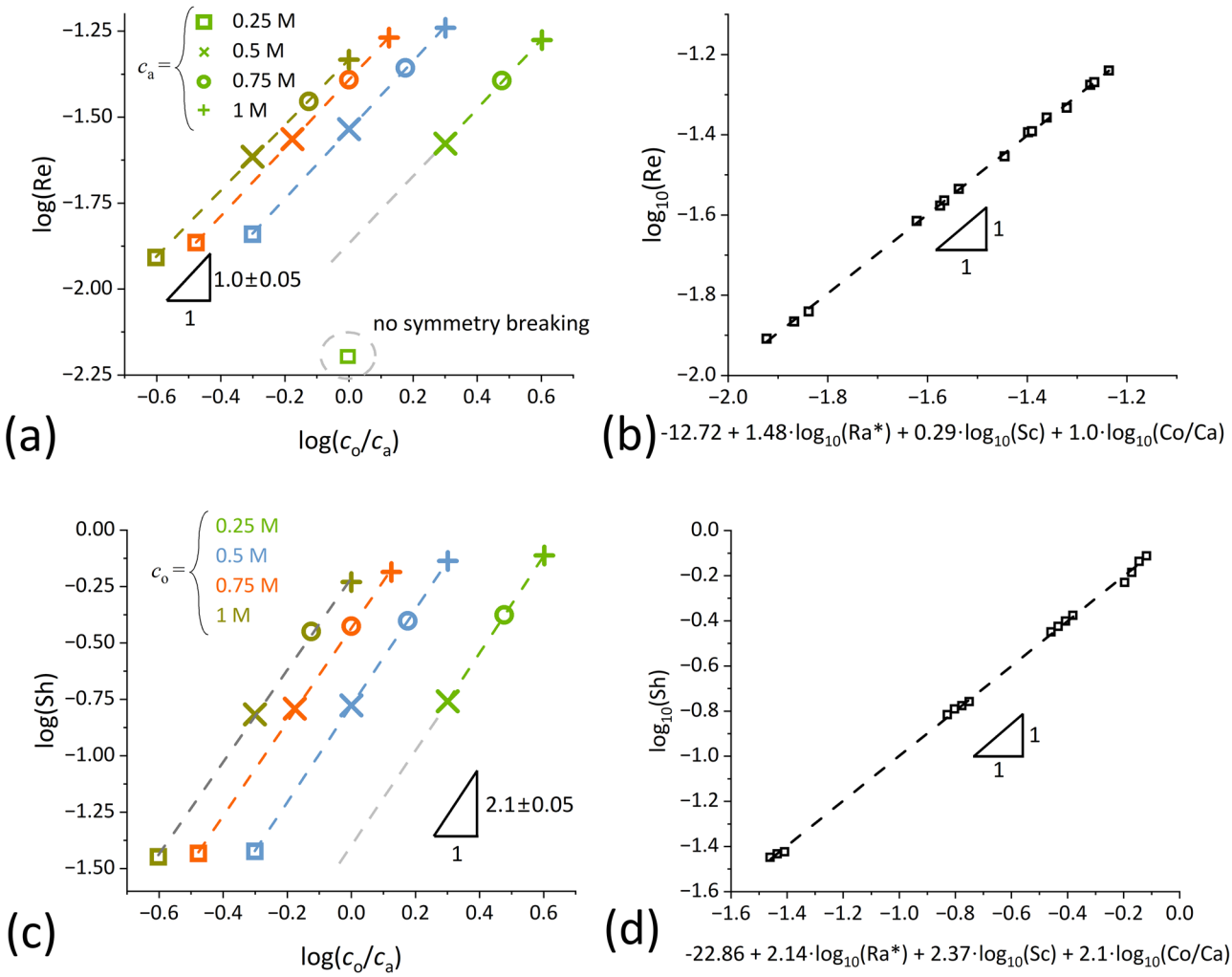

Fig. 6 | Scaling of Re and Sh in solutomagnetic convection. The scaling of Re and Sh with respect to the concentration ratio $\frac{c_o}{c_a}$, Ra^* and Sc is shown in double logarithmic representations. **a**, **c** display the power-law dependence of Re and Sh on the concentration ratio, where symbol colors and shapes represent c_o and c_a, respectively, as indicated in the legends. A unified scaling law for Re and Sh is obtained in (**b**, **d**), respectively, where incorporation of the concentration ratio collapses all data points onto a single fitting curve shown along the abscissa.

The mass transfer scaling law, Eq. (11), is a key result of this work. It quantifies the enhancement of the extraction kinetics for RE(III) ions in presence of the magnetic field, expressed via the Rayleigh number Ra^*, at given c_o/c_a and Schmidt number, *Sc*. As $Ra^* \propto \nabla B^2$, this scaling law for the Sherwood number predicts an average extraction rate to scale according to $\partial_t < c > \propto (\nabla B^2)^{2.14}$. Thus, a doubling of the magnetic field $|B|$ leads to an 18.4-fold acceleration of the Dy(III) extraction kinetics. This demonstrates the importance of the symmetry breaking that takes place when the system operates to the right of the dashed line separating the blue and black data clouds in the $Ra^* - c_o/c_a$ diagram (Fig. 5b). Below this value, there is a slowing down of the extraction kinetics as diffusion limits the influx of fresh Dy(III) solution to the interface.

Demonstrating the transferability of the Dy(III) results to other rare earths

In the following we show that the results found for Dy(III), and expressed in universal non-dimensional form via the Ra* number, are fully applicable to other rare earths. For this purpose, we present experiments with other trivalent rare-earth ions, carried out in the same setup as sketched in Fig. 1. We use one light rare earth element, Sm(III), and two heavy rare earth elements, Ho(III) and Er(III). The molar magnetic susceptibilities of the three species correspond to 2%, 98% and 78% of that of Dy(III)[27].

Fig. 7 summarizes snapshots of RE(III) concentration boundary layer after the magnet is applied at $t = 0$ s. The highly magnetically susceptible heavy rare earths, Ho(III) and Er(III), show a strong enhancement of the extraction kinetics. The latter is even more pronounced than that reported for Dy(III) before. This is due to the higher ligand concentration (2 M instead of 1 M) and the resulting higher Ra^*. We have deliberately chosen this condition for two reasons: first to showcase that the accelerated kinetics is robust across various magnetically susceptible heavy rare earth metals. Second, to point to the dependence on the concentration. Although the magnetic susceptibility of Er(III) is a bit lower than that of Ho(III), the extraction kinetics in the Er(III) system seems to be faster. This points to the nonlinear effects of reaction kinetics, depending on the concentration, which also need to be taken into account.

In contrast, the reaction in Sm(III) is still diffusion-limited with no accelerated extraction kinetics. For the less magnetically susceptible Sm(III), the resulting $Ra^* \approx 3 \times 10^5$ is smaller than Ra^*_{cr}. Therefore, no pronounced solutomagnetic convection can develop in the Sm(III) solution, and hence no enhancement of the extraction kinetics takes place. To achieve the latter, the Kelvin force entering Ra^* needs to be increased. We note that a tiny Sm(III) concentration boundary layer maybe generated when the initial convective field, induced by oil droplet dispersion, is significant. However, this effect no longer has any influence on the results over longer periods.

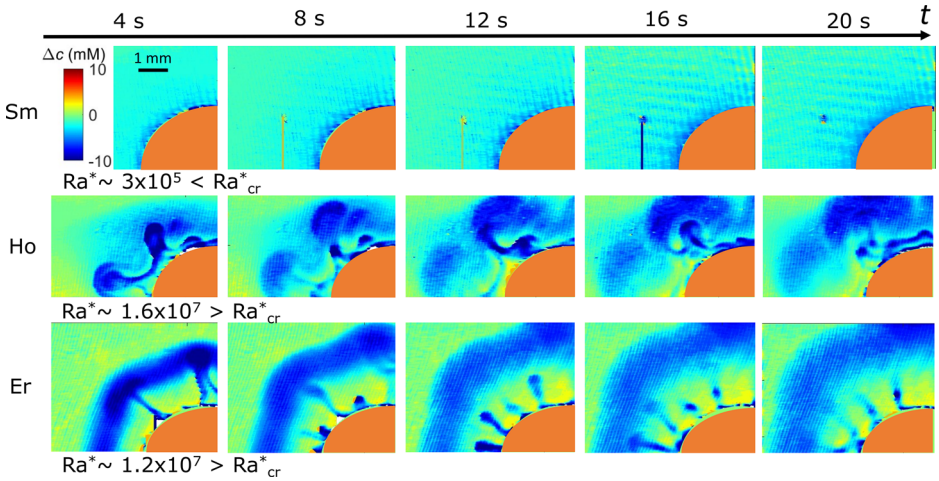

Fig. 7 | Sm(III), Ho(III) and Er(III) extraction kinetics by tailored magnetic fields. RE(III) concentration boundary layer development 20 sec after the magnet is applied to Sm(III), Ho(III) and Er(III) solutions with initial concentration of 1 M. The magnetic field and measurement system used is the same in Fig. 1. A PC88A concentration of 2 M is used for the heavy rare earths, Er(III) and Ho (III); whereas 1 M for both PC88A and Sm(III) is used for the less magnetically susceptible light rare earth Sm(III). The color bar spans the range -10 to 10 mM, while the black line represents the scale bar of 1 mm. They are identical for all three RE(III) species and are referenced to the Sm(III) distribution at 4 s.

Conclusions

This work demonstrates the general principles governing the extraction behavior of trivalent RE ions in a magnetic field gradient. It is important to mention that similar principles also apply to stripping. The latter refers to the backward reaction in Eq. (1), in which the rare earth ions are released into aqueous phase. To achieve the required symmetry break, a magnetic field gradually increasing with distance from the interface is needed here. This is necessary, because the concentration boundary layer is enriched with Dy(III) instead of being depleted, as is the case in the present extraction case. Thus, a ring magnet, instead of a rod magnet, placed concentrically to the oil droplet, can give rise to a positive Ra*, exceeding the critical Ra* of the system, to stimulate a solutomagnetic convection that enhances stripping kinetics.

To sum up, we have achieved a fundamental understanding of the physical mechanisms by means of which magnetic separation can be integrated into solvent extraction. Specifically, we have established a dimensionless group Ra*, Eq. (8), to account for the Kelvin force in solutomagnetic convection, responsible for the reaction kinetics enhancement. The criterion for the onset of advective mass transfer is given by $Ra^* > Ra^*_{cr}$. The critical Ra* value was determined to be $Ra^*_{cr} \sim 5 \times 10^6$ (Fig. 5), which is in excellent agreement with the experiments. Furthermore, we have demonstrated that the resulting extraction kinetics can be enhanced by a magnetic field; even that of a small fingertip magnet is sufficient. We have quantified the effect of magnetic field on extraction kinetics enhancement in terms of the Sherwood number (Eq. (9)). In detail, we were able to show that $Sh \sim Ra^{*2.14}$ holds (Eq. (11)), i.e., Sh follows a quasi-quadratic dependence on Ra*. In the next step the performance increase needs to be quantified in terms of the separation factor, based on well defined experiments using RE(III) mixtures. The basic hypothesis is that the extraction also becomes more selective as the extraction kinetics of the RE's with higher magnetic susceptibility should be more accelerated than that of the RE's with lower magnetic susceptibility. Thus, an enhanced separation factor is predicted for up-scaled apparatuses with an intelligent integration of the magnetic field. Hence, batch or continuous extraction could run under lower consumption of energy and chemicals. The resulting reduction of costs would also make the recycling of REs from their end-of-life products more attractive.

Methods

Material

The aqueous phase was prepared by dissolving dysprosium chloride hexahydrate (99,9 % purity, abcr GmbH) in 0.1 M HCl. The concentrations were adjusted to 0.25 M, 0.5 M, 0.75 M and 1 M, resulting in corresponding kinematic viscosities of 1.024, 1.178, 1.377 and 1.619 mm^2/s. The pH value of the aqueous phase is approximately 1, and the mass diffusivity is $1 \times 10^{-9}\ m^2/s$. The extractant, PC88A (HEHEHP, Combi-Blocks Inc.), was dissolved at similar concentrations between 0.25 M and 1 M in the organic phase, a low-viscosity paraffin (Supelco CAS: 8012-95-1), which has a density of $0.864 \pm 0.002\ g/cm^3$ and a viscosity of 155.3 mm^2/s. Buoyancy neutral 7.7 μm tracer particles (PMMA-FluoRot, microParticles GmbH) were added for the PIV measurement. The reported densities and viscosities were measured with SVM 3001 (Anton Paar). The Dy(III) concentration was verified after preparation using a UV-Vis spectrometer (Shimadzu UV-2700).

Experimental setups

The experiments were conducted in 1 mm thick quartz glass cuvettes (Hellma GmbH & Co. KG, type 101-1-40), with a 1.25 mm wall thickness. The cuvettes were thoroughly rinsed with the aqueous phase used in the experiment so that a homogeneous initial concentration is guaranteed. Afterwards, the cuvettes were filled with the Dy(III)-laden aqueous phase. As soon as the organic droplet was dispersed to a diameter of 4–5 mm inside this aqueous phase, using a non-magnetic, sharp-tipped cannula (0.5 mm diameter) made of stainless steel, the cation exchange spontaneously takes place according to Eq. (1). The resulting Dy(III) concentration boundary layer was measured using a monochromatic Mach-Zehnder Interferometer[24,37] with a 632.8 nm frequency-stabilized He-Ne laser (Research Electro-Optics Inc (REO) Model: 32734). The cuvettes were placed horizontally inside the measurement beam of the interferometer.

Approximately 6...16 s after the droplet was created, a cylindrical permanent NdFeB rod magnet (diameter 4 mm, length 5 mm) with a magnetization strength of N45 (remanence 1.33 T) (Webcraft GmbH) was placed above the cuvette, concentric to the organic droplet. The particle image velocity (PIV) system used a microscope lens (Carl-Zeiss) to focus the laser beam onto the cuvette and to record the image. A Nd:Yag laser, 1 kHz, 527 nm wavelength, generates pulses that excite the fluorescent particles. As a result, the fluorescent particles emit excitation light with longer wavelength, following Stokes shift, that passes through a long-pass filter so that the particle trajectories can be captured with the camera. The cameras ROI is further divided into partially overlapping interrogation windows. PIV data processing, which is based on the cross-correlation of particle positions within a fixed interrogation window at adjacent time steps, is performed using the DaVis software (LaVision DaVis 10.2) to calculate the local flow velocity and the space-averaged kinetic energy.

Similarity measure

To describe the symmetry breaking event quantitatively, we conduct time-resolved similarity measures for the Dy(III) concentration stratification along the radial direction between different angular positions ϕ. Please refer to Fig. 1, center, for the cylindrical coordinate system. Axial symmetry is evaluated by quantifying the total area enclosed by the concentration

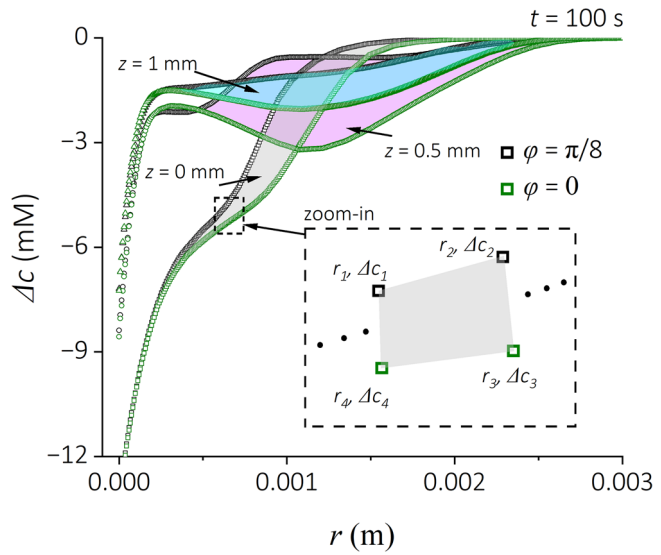

Fig. 8 | Similarity measure. Sampling of concentration depletion, Δc, at different angular positions ϕ and depth z. Each pair in $\Delta c - r$ space at same depth encloses an area which is quantified using a discrete sum of the area method. The method summarizes the area enclosed by 4 consecutive sampling points, two discrete sampled points for each angular direction φ, which is shown in close-up. The symmetry breaking level is quantified by the total area that is enclosed by the two sampling lines marked gray, pink and blue for the bottom, middle and top planes, respectively.

stratification between $\phi = 0$ and $\phi = \pi/8$ at the same snapshot. The time stamp at which axial symmetry no longer hold is captured by a discrete sum of the area method[34] in a $\Delta c - r$ space.

A magnified view of each consecutive pair of sampling sequences is plotted in Fig. 8 and marked as r_i, $\Delta c_i (i = 1, 2, 3, 4)$. The 4 points are re-ordered into a non-self-intersecting quadrilateral. Therefore, the total area is equivalent to the summation of each unit area (color gray in Fig. 8 zoom-in) expressed with the triangle formula $< \frac{1}{2}\sum_{i=4}^{i=1}(r_i\Delta c_i + 1 - r_{i+1}\Delta c_i) > \sum$, where $< > ^{\sum}$ denotes a summation of all consecutive quadrilaterals at the depicted time stamp. The quantification of the similarity measure is shown by way of example in Fig. 8 at $t = 100$ s when taking samples from the bottom, middle and top of the solution along the gravitational direction.

Governing equations and Variable table

Table 1 summarizes the variables used throughout the manuscript. The incompressible Navier-Stokes equation, incorporating the Kelvin force $\vec{f}_m$ and buoyancy $\vec{f}_g$, reads

$$D_t(\rho\vec{u}) = -\nabla p + \nabla \cdot (\mu\nabla\vec{u}) + \vec{f}_m + \vec{f}_g. \tag{12}$$

The Kelvin force is expressed as the gradient of the magnetic term of the Gibbs free energy G[1,29]

$$\vec{f}_m = -\nabla G = \nabla(\mu_0\vec{H}\cdot\vec{M}) \tag{13}$$

where $\vec{H}$ and $\vec{M}$ are respectively the external magnetic field and the magnetization, with μ_0 the vacuum permeability. The dilute Dy(III) aqueous solution exhibits a negligible demagnetization field which allows to simplify the Kelvin force into a magnetic field gradient force. Furthermore, since no Lorentz force is present in the system studied, the formulation of Kelvin force in form of a gradient of the magnetic pressure is valid[30], hence

$$\vec{f}_m = \frac{\chi_{\mathrm{sol}}}{\mu_0}(\vec{B}\cdot\nabla)\vec{B} = \frac{\chi_{sol}}{2\mu_0}\nabla\vec{B}^2. \tag{14}$$

Table 1 | List of variables, description and unit

Variable	Description	Unit
$\vec{B}$	magnetic flux density	[T]
c	Dy(III) concentration/ scalar	[M]
c_0	Dy(III) initial concentration	[M]
c_a	Dy(III) concentration	[M]
c_o	PC88A concentration in organic dilute	[M]
c^*	dimensionless Dy(III) concentration/ scalar	[/]
D	mass diffusivity	[m^2/ s]
$\vec{e}_n$	boundary normal unit vector	[/]
$\vec{e}_{-\nabla e_{pot}}$	unit vecotor along $-\nabla e_{pot}$	[/]
e_{pot}	potential energy density field	[J/m^3 · mM]
$\vec{f}_m$	Kelvin Force	[N/m^3]
G	Gibbs free energy	[J/m^3]
$\vec{g}$	gravity vector	$[\frac{m}{s^2}]$
$\vec{H}$	magnetic field	$[\frac{A}{m}]$
L_c	characteristic length	[m]
L^*	dimensionless length	[/]
$\vec{M}$	Magnetization	$[\frac{A}{m}]$
p	pressure	Pa
$p\prime$	reduced pressure	Pa
$\tilde{p}$	dimensionless pressure	[/]
R	Dy(III) mass flux per unit area through interface	[mol/m^2 · s]
r	radial coordinate	[m]
Ra	Rayleigh number	[/]
Ra^*	Rayleigh star number	[/]
Re	Reynolds number	[/]
Sc	Schmidt number	[/]
Sh	Sherwood number	[/]
t	time	[s]
t^*	dimensionless time	[/]
$\vec{u}$	velocity	[m/ s]
$\tilde{\vec{u}}$	dimensionless velocity	[/]
z	z-axis anti-parallel to gravitational direction	[m]
α	densification coefficient	[M^{-1}]
Δc	concentration change	[M]
ϕ	angular axis	[rad]
ρ_c	concentration dependant density	$[\frac{kg}{m^3}]$
ρ_0	initial density	$[\frac{kg}{m^3}]$
χ_{Dy}	Dy(III) molar magnetic susceptibility	[M^{-1}]
χ_{sol}	magnetic susceptibility of solution	[/]
μ_0	vacuum magnetic permeability	[N/A^2]
ν	kinematic viscosity	m^2/s

The Variables are described when they first appear in the manuscript. The subscription Dy is the abbreviation of heavy rare-earth element Dysprosium. PC88A is Mono-2-ethylhexyl (2-Ethylhexyl) phosphonate with CAS number: 14802-03-0.

Due to the mass transfer of Dy(III), the concentration of Dy(III) in the aqueous phase, c, differs from the initial, homogeneous value, c_0, i.e., $c = c_0 + \Delta c$.

Δc gives rise to a non-balanced increment of the body force term

$$\Delta\vec{f}_m + \Delta\vec{f}_g = \rho_0\vec{g} - \nabla e_{pot}\cdot c_0 + \nabla e_{pot}\cdot\Delta c \tag{15}$$

creating a source of vorticity.

$$e_{pot} = -\left(\frac{\chi_{Dy}}{2\mu_0}\cdot\vec{B}^2 + \rho_0 g\alpha\cdot z\right) + \text{const} \tag{16}$$

is the molar potential energy density field introduced in[30]. Applying the Boussinesq approximation, a reduced pressure field, given by

$$p' = p - \rho_0 gz - e_{pot}c_0 \tag{17}$$

is obtained, where $\rho_{c_0} = \rho_0(1+\alpha c_0) = 1475.56\ \text{kg/m}^3$ with $\rho_0 = 997\ \text{kg/m}^3$ - water density and $\alpha = 0.24\ \text{M}^{-1}$ - the solutal volume expansion coefficient[27]. The transport process in the rare-earth solution is governed by the incompressible Navier-Stokes equation in the Boussinesq approximation. For the sake of completeness in equation derivation, we repeat here the dimensional momentum equation

$$\partial_t\vec{u} + \vec{u}\cdot\nabla\vec{u} = -\frac{1}{\rho_{c_0}}\nabla p' + \nu\nabla^2\vec{u} - \frac{1}{\rho_{c_0}}\nabla(e_{pot})\Delta c, \tag{18}$$

together with the advection-diffusion equation for the Dy(III) concentration:

$$\partial_t c + \vec{u}\cdot\nabla c = \kappa_c\nabla^2 c. \tag{19}$$

Inital conditions are $\vec{u} = 0$ and $c = c_0$. The Dy(III) mass boundary condition is expressed as Neumann boundary condition, quantified by $\nabla c\cdot\vec{e}_n = R/D$ with $\vec{e}_n$ referring to the normal unit vector at interface. The Dy(III)-flux per interfacial area, R, at the organic-aqueous interfaces is calculated at each time stamp via a semi-empirical forward rate law quantifying the Dy(III) mass-flux to be introduced shortly. The numerical domain considers the Dy(III) aqueous solution similar to that studied experimentally. The same cylindrical coordinate system is used as defined in Fig. 1, middle insertion. The z-axis is anti-parallel to gravitational acceleration vector. The length considered in z direction has an extension of 1 mm. In the radial direction the domain extends over $r \in [2\ \text{mm}, 10\ \text{mm}]$ where the inner wall at $r = 2$ mm represents the oil-water interface. A no-slip boundary condition is used for all walls except for the vertical inner wall where a simplification of Navier's slip boundary is used. One major challenge is that no analytical slip length λ is known for an immiscible liquid-liquid interface. This is due to the presence of the two momentum dissipation scales in the respective phases which have identical density and finite viscosity ratio (unlike air-liquid and solid-liquid systems, which have viscosity ratios asymptotic to 0 and infinity, respectively.). An identical case from literature[38] derives uniform steady-state slip length from a spherical droplet in water under Stokes flow condition. Hence, a constant slip length in form $\lambda = \frac{R}{3\mu^*}$ is used instead where $\mu^* = \mu_o/\mu_a$ is the dynamic viscosity ratio between organic and aqueous phase. The simulations are conducted using the open-source software OpenFOAM at a cylindrical domain with a hexahedral unstructured mesh that has an interface mesh size of $\approx 1.05\ \mu$m at the inner vertical wall representing the interface.

A review of the literature revealed no reliable kinetic law for the Dy(III) reaction that takes into account both the forward and backward reactions. Therefore, a semi-empirical forward rate law is used[39]

$$R = 7.7\times10^{-4}[Dy(III)]^{1.1}[H_2A_2]^{2.3} \tag{20}$$

where the square brackets represent the concentration of the species. The omission of the backward reaction term in the kinetic rate law introduces an over-estimation of the Dy-boundary flux at the extraction stage close to equilibrium. This simplification is valid for the time span considered. The good agreement between the measured transport processes with that simulated within the time span of the experiment further confirms the validity. However, the inclusion of backward reaction kinetics term would be necessary for stripping process or extraction/ stripping close to equilibrium, which is beyond the scope of the present work.

Scaling factors and dimensionless governing equations

With the length L_c, the diffusion time $\frac{L_c^2}{D}$ and the initial concentration c_0 as characteristic scales, the dimensionless variables read $\widetilde{L} = L/L_c$; $\widetilde{t} = t/\frac{L_c^2}{D}$; $\widetilde{\vec{u}} = u/\frac{D}{L_c}$ and $\widetilde{c} = c/c_0$. Thus the source term on the right-hand side of Eq. (15), scaled with $\left(\frac{L_c^2}{D}\right)/(L_c\cdot Sc)$, is given by

$$\frac{L_c^3\cdot c_0|\nabla e_{pot}|}{\rho_{c_0}\cdot\nu D}\cdot\widetilde{c}\cdot\vec{e}_{-\nabla e_{pot}} = \text{Ra}^*\cdot\widetilde{c}\cdot\vec{e}_{-\nabla e_{pot}} \tag{21}$$

where the $\vec{e}_{-\nabla e_{pot}}$ is the unit vector of $-\nabla e_{pot}$ and the multiplier at the left-hand side of the equation is the dimensionless Ra* number. Non-dimensionalizing Eq. (4), we obtain the dimensionless momentum equation correlating dimensionless velocity $\widetilde{\vec{u}}$, pressure $\widetilde{p}$ and concentration: $\widetilde{c}$

$$\frac{1}{Sc}(\partial_t\widetilde{\vec{u}} + \widetilde{\vec{u}}\cdot\nabla\widetilde{\vec{u}}) = -\nabla\widetilde{p} + \nabla^2\widetilde{\vec{u}} + \text{Ra}^*\widetilde{c}\,\vec{e}_{-\nabla e_{pot}}. \tag{22}$$

The same applies for the scalar transport equation

$$\partial_t\widetilde{c} + \widetilde{\vec{u}}\cdot\nabla\widetilde{c} = \nabla^2\widetilde{c}. \tag{23}$$

As already mentioned before, at vanishing magnetic flux density, Ra^* is reduced to the conventional Ra number, $\text{Ra} = \frac{L_c^3 g\Delta\rho}{\rho_{c_0}\nu D}$ where $\Delta\rho$ refers to $\Delta\rho = \rho_0\alpha\Delta c$. This elegance also applies for the $\vec{e}_{-\nabla e_{pot}}$, which is reduced to gravity unit vector. Therefore, this dimensionless set of equations converges to that used in Rayleigh-Bénard convection (RBC) at zero magnetic field $\vec{B}$.

The magnetic energy introduced into the system can be decreased by increasing the distance between the magnetic pole and the cuvette wall. To be specific, an increase by a distance of 1.5 mm, reduces e_{pot} by 18 times, see Fig. 9. We use this variation of the distance as a tool to resolve the symmetry break and to specify the critical Ra^* number where it occurs.

Kinetic energy calculation

The experimental kinetic energy was calculated based on the velocity data from the PIV experiments according to $e_{kin} = <1/2v^2>$ to compare with that obtained numerically. Since the vortices in the flow field do not protrude beyond the measurement region over the observed time period, the error caused by this constraint can be ignored. Numerically, a variation in e_{kin} is found at different initial Dy(III) and PC88A concentrations, see Fig. 3c. The characteristic velocity in the Reynolds number is derived readily from quasi-steady state average kinetic energy in terms of $\sqrt{2e_{kin}}$.

A variety of factors can contribute to the error bar of the kinetic energy computed from PIV measurements, cf. Fig. 3c. These include minor technically related initial velocity perturbations caused by e.g. droplet dispersion and the cannule withdrawal. In addition, the droplet size varies to a small degree in most cases between 3.9 and 4.5 mm. However, no differences in the number of developing vortex pairs were observed based purely on the droplet size. When the magnet is applied, there is an uncertainty of around ±0.3 mm in the displacement between the center of the magnet and the center of the droplet. Nevertheless, the vortices generated by the resulting, slightly deviating magnetic field are similar in length with a marginal variation in intensity. The curved meniscus blocks direct optical access, preventing a direct optical access to the interface and the ca. 0.4 mm thick layer surrounding the interface, where the velocity reaches a maximum. Furthermore, at longer time spans, the vicinity of the interface is gradually

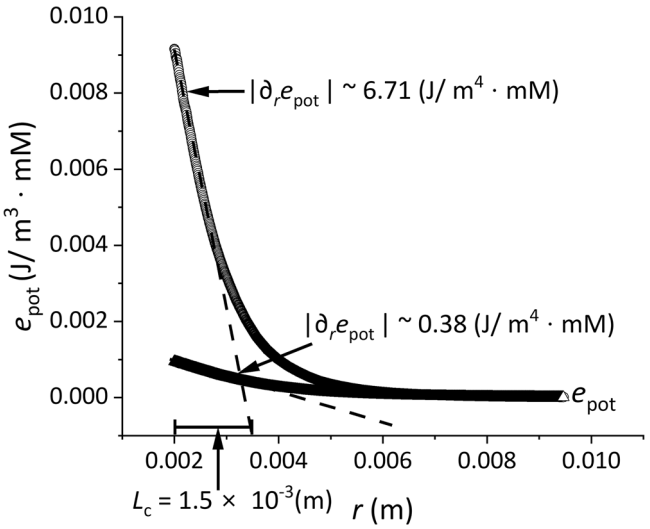

Fig. 9 | Potential energy density e_{pot} of the magnet. Upon introducing a 1.5 mm gap between the magnet pole and the cuvette wall, the gradient drops from 6.71 J/m^4 · mM to 0.38 J/m^4 · mM.

depleted with tracing particles. This leads to an increased level of underestimation of the kinetic energy in the direct vicinity of the oil-water interface. This is the major reason for smaller average kinetic energy measured experimentally compared to that simulated in Fig. 3c.

Data availability

Raw data used to generate the figures of this manuscript are published and available at figshare with DOI 10.6084/m9.figshare.30323215.v1. Further data that support the findings of this study are available from corresponding author Zhe Lei upon reasonable request.

Received: 18 June 2025; Accepted: 24 October 2025;
Published online: 07 November 2025

References

1. Coey, J. *Magnetism and Magnetic Materials* Illustrated edition, Vol. 625 (Cambridge University Press, Cambridge, 2010).
2. Waske, A. et al. Energy harvesting near room temperature using a thermomagnetic generator with a pretzel-like magnetic flux topology. *Nat. Energy* **4**, 68–74 (2019).
3. Zhang, S. et al. Rare-earth incorporated alloy catalysts: Synthesis, properties, and applications. *Adv. Mater.* **33**, 2005988 (2021).
4. Li, S., Zhou, L. & Zhang, H. Investigation progresses of rare earth complexes as emitters or sensitizers in organic light-emitting diodes. *Light Sci. Appl.* **11**, 177 (2022).
5. Zhang, H. & Zhang, H. Rare earth luminescent materials. *Light Sci. Appl.* **11**, 260 (2022).
6. Balaram, V. Rare earth elements: A review of applications, occurrence, exploration, analysis, recycling, and environmental impact. *Geosci. Front.* **10**, 1285–1303 (2019).
7. Nations, U. *Framework Convention On Climate Change (2015) Adoption Of The Paris Agreement,21st Conference Of The Parties, Paris: United Nations*. https://unfccc.int (2015).
8. Binnemans, K., McGuiness, P. & Jones, P. T. Rare-earth recycling needs market intervention. *Nat. Rev. Mater.* **6**, 459–461 (2021).
9. Cordier, D. J. *Rare Earths Statistics and Information*. https://www.usgs.gov/centers/national-minerals-information-center/rare-earths-statistics-and-information (2023).
10. Beylot, A. et al. Economic assessment and carbon footprint of recycling rare earths from magnets: Evaluation at lab scale paving the way toward industrialization. *J. Ind. Ecol.* **24**, 128–137 (2020).
11. Xie, F., Zhang, T. A., Dreisinger, D. & Doyle, F. A critical review on solvent extraction of rare earths from aqueous solutions. *Mineral Eng.* **56**, 10–28 (2014).
12. Ali, S. H. Social and environmental impact of the rare earth industries. *Resources* **3**, 123–134 (2014).
13. Geng, Y., Sarkis, J. & Bleischwitz, R. How to build a circular economy for rare-earth elements. *Nature* **619**, 248–251 (2023).
14. Peppard, D., Mason, G., Maier, J. & Driscoll, W. Fractional extraction of the lanthanides as their di-alkyl orthophosphates. *J. Inorg. Nucl. Chem.* **4**, 334–343 (1957).
15. Peppard, D., Faris, J., Gray, P. & Mason, G. Studies of the solvent extraction behavior of transition elements. i. order and degree of fractionation of the trivalent rare earths. *J. Phys. Chem.* **57**, 294–301 (1953).
16. Marx, J., Schreiber, A., Zapp, P. & Walachowicz, F. Comparative life cycle assessment of ndfeb permanent magnet production from different rare earth deposits. *ACS Sustain. Chem. Eng.* **6**, 5858–5867 (2018).
17. Binnemans, K., Jones, P. T., Blanpain, B., Van Gerven, T. & Pontikes, Y. Towards zero-waste valorisation of rare-earth-containing industrial process residues: a critical review. *J. Cleaner Product.* **99**, 17–38 (2015).
18. Cheisson, T. & Schelter, E. J. Rare earth elements: Mendeleevs bane, modern marvels. *Science* **363**, 489–493 (2019).
19. Binnemans, K. & Jones, P. T. Solvometallurgy: an emerging branch of extractive metallurgy. *J. Sustain. Metall.* **3**, 570–600 (2017).
20. Bonificio, W. D. & Clarke, D. R. Rare-earth separation using bacteria. *Environ. Sci. Technol. Lett.* **3**, 180–184 (2016).
21. Fang, H. et al. Electro-kinetic separation of rare earth elements using a redox-active ligand. *Angew. Chemie.* **129**, 13635–13639 (2017).
22. Traore, M. et al. Research progress of rare earth separation methods and technologies. *J. Rare Earths* **41**, 182–189 (2023).
23. Franczak, A., Binnemans, K. & Fransaer, J. Magnetomigration of rare-earth ions in inhomogeneous magnetic fields. *Phys. Chem. Chem. Phys.* **18**, 27342–27350 (2016).
24. Lei, Z., Fritzsche, B. & Eckert, K. Evaporation-assisted magnetic separation of rare-earth ions in aqueous solutions. *J. Phys. Chem. C* **121**, 24576–24587 (2017).
25. Benhal, P. et al. Dynamics of transition metal ion transport in high-gradient magnetic fields. *J. Phys. Chem. A* **129**, 3401–3410 (2025).
26. Kumar, A., Geng, H. & Schelter, E. J. Harnessing magnetic fields for rare-earth complex crystallization–separations in aqueous solutions. *RSC Adv.* **12**, 27895–27898 (2022).
27. Lei, Z. et al. Magnetic separation of rare-earth ions: property database and kelvin force distribution. *J. Phys. Chem. C* **126**, 2226–2233 (2022).
28. Mason, G., Bilobran, I. & Peppard, D. Extraction of u (vi), th (iv), am (iii) and eu (iii) by bis para-octylphenyl phosphoric acid in benzene diluent. *J. Inorg. Nucl. Chem.* **40**, 1807–1810 (1978).
29. Rosensweig, R. E. *Ferrohydrodynamics* Vol. 344 (Courier Corporation, 2013).
30. Lei, Z., Fritzsche, B. & Eckert, K. Stability criterion for the magnetic separation of rare-earth ions. *Phys. Rev. E* **101**, 013109 (2020).
31. Ahlers, G., Grossmann, S. & Lohse, D. Heat transfer and large scale dynamics in turbulent rayleigh-bénard convection. *Rev. Modern Phys.* **81**, 503 (2009).
32. Keane, R. D. & Adrian, R. J. Theory of cross-correlation analysis of piv images. *Appl. Sci. Res.* **49**, 191–215 (1992).
33. Lei, Z., Fritzsche, B. & Eckert, K. Magnetic separation of rare-earth ions: transport processes and pattern formation. *Phys. Rev. Fluids* **6**, L021901 (2021).
34. Jekel, C. F., Venter, G., Venter, M. P., Stander, N. & Haftka, R. T. Similarity measures for identifying material parameters from hysteresis loops using inverse analysis. *Int. J. Mater. Forming* **12**, 355–378 (2019).

35. Gupta, A., Rallabandi, B. & Stone, H. A. Diffusiophoretic and diffusioosmotic velocities for mixtures of valence-asymmetric electrolytes. *Phys. Rev. Fluids* **4**, 043702 (2019).
36. Lim, B. et al. Magnetophoretic circuits for digital control of single particles and cells. *Nat. Commun.* **5**, 3846 (2014).
37. Ghiglia, D. C. & Pritt, M. D. *Two-dimensional Phase Unwrapping: Theory, Algorithms, And Software*, Vol. 512 (Wiely-Interscience, 1998).
38. Legendre, D., Rachih, A., Souilliez, C., Charton, S. & Climent, É. Basset-boussinesq history force of a fluid sphere. *Phys. Rev. Fluids* **4**, 073603 (2019).
39. Sun, F., Ortmann, K., Eckert, K. & Lei, Z. Interferometric measurement of forward reaction rate order and rate constant of a dy(iii)-pc88a-hcl solvent extraction system. In *Magnetic Microhydrodynamics: An Emerging Research Field*, 131–140 (Springer series: Topics in Applied Physics., Gewerbestrasse 11, 6330 Cham, Switzerland, 2024).

Acknowledgements

We thank the German Aerospace Center (DLR) for the financial support by funds provided by the Federal Ministry for Economic Affairs and Energy (BMWi) due to an enactment of the German Bundestag under Grant No. DLR 50WM2059 and 50WM2359 (Project MAGSOLEX). We are grateful for the valuable comments by Prof. Jean-Claude Bünzli on our work. We thank Yuheng He for his active support in developing the experimental protocol used to address the reviewers' comments.

Author contributions

Z.Lei conceived the project. Z.Lei and K.Eckert acquired the funding. K.Ortmann and Z.Lei designed the work. K. Ortmann, A. Bidmon performed the work with the support of K. Eckert and Z. Lei. K. Ortmann performed data evaluation and their analyses with the support of Z. Lei. All authors contributed to writing of the manuscript. All authors reviewed and approved the publication of this manuscript.

Funding

Open Access funding enabled and organized by Projekt DEAL.

Competing interests

The authors declare no competing interests.

Additional information

Supplementary information The online version contains supplementary material available at https://doi.org/10.1038/s42005-025-02393-7.

Correspondence and requests for materials should be addressed to Zhe Lei.

Peer review information *Communications Physics* thanks Jean-Claude Bünzli and the other, anonymous, reviewer(s) for their contribution to the peer review of this work. A peer review file is available.